AEÜ International Journal of Electronics and Communications

Aperture-Radiated Electromagnetic Field Synthesis in Complex Environments via Narrow-Waisted Gabor-Discretized Gaussian Beams

Leopold B. Felsen and Vincenzo Galdi

Dedicated to Professor Peter Russer on the occasion of his 60th birthday

Abstract: This review deals with the utility, scope, performance, and range of validity of the discretized Gabor-based, quasi-ray, narrow-waisted (NW) Gaussian beam (GB) algorithm for the analysis and synthesis of high frequency time-harmonic as well as short-pulse transient electromagnetic wavefields in the presence of complex propagation and scattering environments. Restricting attention here primarily to two-dimensional (2-D) fields and physical configurations, applications include phased and focused truncated plane-aperture-generated illumination of layered dielectrics, moderately rough air-soil interfaces, and buried objects in rough-surface-bounded halfspaces in forward scattering scenarios, as well as rough interface profile reconstruction and buried-target imaging from sparse data in inverse scattering scenarios. The role of the Gabor-based NW-GB algorithm as a computationally efficient physically incisive analytic forward solver in these applications is emphasized. Current status is reviewed and assessed in detail, with brief discussion of plans for future extensions, and of recently developed alternative methodologies.

Keywords: Gaussian beams, Gabor discretization, Propagation, Forward scattering, Inverse scattering

1. Introduction

The objective, scope, and range of applications in this review of the Gabor-based, quasi-ray, narrow-waisted (NW) Gaussian beam (GB) algorithm for the representation of (primarily) two-dimensional (2-D) electromagnetic (EM) wavefields generated by time-harmonic high frequency as well as short-pulse transient excitations from rather general truncated plane 1-D aperture field distributions in the presence of 2-D complex propagating and scattering environments has been summarized in the abstract, and need not be repeated here. Instead, we procede directly to the structure of the paper. The presentation is divided into three principal sections: Sect. 2: Forward Scattering; Sect. 3: Inverse Scattering; Sect. 4: Current and Planned Investigations, and Alternative Approaches.

Section 2 is the most comprehensive, and contains four subsections, 2.1, 2.2, 2.3, 2.4, each of which is divided into two parts: 1. Frequency domain (FD); 2. Time domain (TD). The four subsections are entitled: 2.1. Plane-Aperture Radiation; 2.2. Transmission/Reflection Due to Layered Dielectrics; 2.3. Transmission/Reflection Due to Moderately Rough Dielectric Interfaces; 2.4. Scattering by Objects Embedded Below Moderately Rough Dielectric Interfaces. Section 2.1 is the "driver" that provides both the rigorously phrased Kirchhoff-integral and the approximate Gabor NW-GB discretized expansions for the 2-D incident fields that illuminate the 2-D environments in Sects. 2.2, 2.3, 2.4. The Gabor lattice in the (spatial)-(wavenumber spectral) phase space, which parameterizes the 1-D aperture field and thereby the radiated 2-D GB propagators, is introduced at this stage, together with its special properties in the NW-ray-like regime that permits evaluation of the formally messy Gabor amplitude coefficients by mere sampling of the aperture profile at the lattice points within the aperture domain; the tight spatial packing under NW conditions gives rise to wide spectral spacing (i.e., large "tilt" intervals) due to the Gabor spatial-spectral tradeoff, which drives all tilted beams away from the aperture into the evanescent range. Thus, the NW-GB synthesis of the radiated field involves only an aperture-filling finite series of propagating beams, even for the phased aperture distributions. The NW-GB expansions for the wavefield environmental encounters in Sects. 2.2, 2.3, 2.4 are synthesized very efficiently by "quasi-ray" tracking of each incident nontilted basis beam through the environment and combining at the observer; the slightly complex quasi-ray propagators do not encounter the failures of real ray fields in transition regions. For each application, the validity of the NW-GB synthesized fields is assumed to be established through the "scrambling" criterion, which regards the synthesis as stabilized when finer samplings (i.e., more beams with narrower waists) do not alter the result. Each such application has to be validated independently by comparison with brute-force computationally intensive reference solutions, thereby establishing its range of applicability. Concerning the FD vs. TD regimes, we usually start with the FD and access the short-pulse TD by "analytic" inversion from the FD, with efforts to structure

Received August 22, 2002. Revised November 22, 2002.

L. B. Felsen, Department of Aerospace and Mechanical Engineering, Boston University, 110 Cummington St., Boston, MA 02215, USA (part-time). Also, University Professor Emeritus, Polytechnic University, Brooklyn, NY 11201, USA. E-mail: lfelsen@bu.edu
V. Galdi, Department of Engineering, University of Sannio, Palazzo Dell'Aquila Bosco Lucarelli, Corso Garibaldi 107, I-82100 Benevento, Italy. E-mail: vgaldi@unisannio.it

Correspondence to V. Galdi.

the pulse spectrum in such a way as to admit approximate closed forms for the TD NW pulsed beam (PB) wavepackets; the analytic (positive frequency) transform accommodates the weakly evanescent spectra of the NW-GBs. Each application is accompanied by a compact analytic portion which deals with the relevant basis beam tracking algorithms, and by a typical numerical example that shows the performance capabilities of the GB synthesis for the specified "sufficient" number of beams.

The inverse scenarios in Sect. 3 involve: 3.1. Overall Problem Strategy; 3.2. Reconstruction of the Moderately Rough Dielectric Interface Profile; 3.3. Imaging of Targets Buried Below the Moderately Rough Dielectric Interface. The inversion strategies are structured around the corresponding NW-GB discretizations in Sect. 2 as noted earlier. Section 4 deals in brief summary form with current and planned extensions of the NW-GB algorithms to full 3-D geometries; alternative methodologies, not based on Gabor discretization, are also given attention. Section 5 contains brief conclusions.

Concerning notation, bold face symbols denote vector quantities; light face symbols denote scalar quantities; capital letter fields are set in the FD; lower-case-letter fields are set in the TD; a tilde $\tilde{}$ superscript on a quantity denotes its extension into a complex coordinate space; superscript $^+$ denotes the analytic temporal Fourier transform (FT); the caret $\hat{}$ denotes plane-wave spectral domain functions. Frequently used abbreviations throughout the paper are: GB = Gaussian beam; NW = narrow-waisted; PB = pulsed beam; CSP = complex source point; FD = frequency domain; TD = time domain; TM = transverse magnetic; PO = physical optics; GPR = ground penetrating radar; TV = total variation; CE = curve evolution.

2. Forward scattering

2.1 Plane-aperture radiation

2.1.1 Frequency domain

Consider a two-dimensional problem where a $y-$directed electric field with implicit time-harmonic dependence $\exp(-i\omega t)$ and spatial distribution $F(x)$ is assumed to occupy the aperture region $|x| \le d/2$ at $z = 0$, as depicted in Fig. 1,

$$E_y(x, z = 0) = F(x), \quad |x| \le d/2\,. \tag{1}$$

The resulting EM field radiated into the halfspace $z > 0$ can be expressed as a superposition of line-source-generated fields (Kirchhoff integration) [1]

$$E_y(\mathbf{r}) = -2\frac{\partial}{\partial z}\int\limits_{-d/2}^{d/2} F(x')G_{2D}\big(\mathbf{r};\mathbf{r}'_0;k_0\big)dx'\,, \tag{2}$$

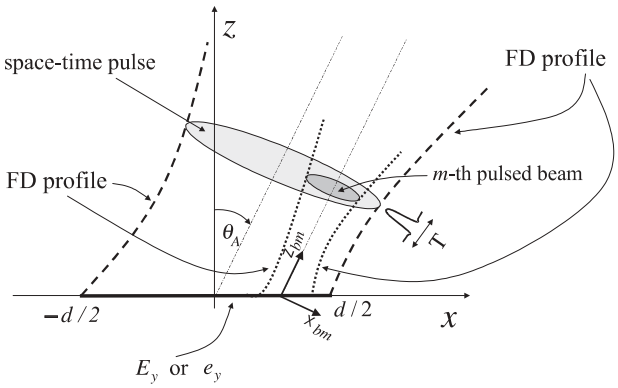

Fig. 1. Problem geometry pertaining to Sect. 2.1: frequency or time domain. A wavefield emanates from an extended truncated aperture field distribution at $z = 0$.

where $\mathbf{r} \equiv (x, z)$; $\mathbf{r}'_0 \equiv (x', 0)$ denotes points on the aperture plane, $k_0 = \omega\sqrt{\epsilon_0\mu_0} = 2\pi/\lambda_0$ is the free-space wavenumber, λ_0 is the free-space wavelength, and G_{2D} is the FD 2-D Green's function

$$G_{2D}\big(\mathbf{r};\mathbf{r}';k_0\big) = \frac{i}{4}H_0^{(1)}\big(k_0|\mathbf{r}-\mathbf{r}'|\big)\,, \tag{3}$$

with $H_0^{(1)}(\cdot)$ denoting the zeroth order Hankel function of the first kind [2]. Alternatively, by spectral plane wave superposition, one obtains [1]

$$E_y(\mathbf{r}) = \frac{1}{2\pi}\int\limits_{-\infty}^{\infty}\hat{F}(k_x)\exp\big[i\,(k_x x + k_z z)\,\big]dk_x\,, \tag{4}$$

where

$$\hat{F}(k_x) = \int\limits_{-\infty}^{\infty} F(x)\exp(-ik_x x)dx \tag{5}$$

is the Fourier plane-wave spectrum of $F(x)$, k_x is the x-domain wavenumber, and

$$k_z = \sqrt{k_0^2 - k_x^2}, \quad \mathrm{Im}(k_z) \ge 0\,, \tag{6}$$

is the longitudinal (z-domain) wavenumber.

The aperture field $F(x)$ is to be parameterized in terms of Gaussian basis functions via the rigorous self-consistent Gabor series representation [3–5]

$$F(x) = \sum_{m,n=-\infty}^{\infty} A_{mn}\,w(x - mL_x)\exp(in\beta_x x)\,, \tag{7}$$

$$L_x\beta_x = 2\pi\,,$$

where $w(x)$ represents the normalized Gaussian window function

$$w(x) = \left(\frac{\sqrt{2}}{L_x}\right)^{1/2} \exp\left[-\pi(x/L_x)^2\right], \qquad \int_{-\infty}^{\infty} w^2(x)dx = 1\,, \tag{8}$$

and spatial/spectral periods are related by the self-consistency condition (configuration-spectrum tradeoff) in the second equation of (7) [3]. The representation in (7) places the aperture distribution on a discretized (x, k_x) phase space lattice (see Fig. 2), with spatial/spectral shifts tagged by the indexes m and n, respectively. The initial windowed distribution surrounding each lattice point in Fig. 2 generates a Gaussian beam (GB) which is launched from m-indexed locations and tilted according to n-indexed locations. The radiated incident field in the halfspace $z > 0$ (see (2)) therefore admits via (7) a similar discretized representation,

$$E_y(\mathbf{r}) = \sum_{m,n=-\infty}^{\infty} A_{mn} B_{mn}(\mathbf{r})\,, \tag{9}$$

where the beam functions $B_{mn}(\mathbf{r})$ in the *paraxial far zone* can be expressed via the following *complex source point* (CSP) approximation [6, 7]

$$B_{mn}(\mathbf{r}) \sim \tilde{B}_{mn}(\mathbf{r}) = -ik_0 2^{5/4}\left(\frac{L_x}{8\pi k_0}\right)^{1/2} \times \exp\left\{i\left[k_0\left(\tilde{R}_{mn} + ib\right) + \pi/4\right]\right\} \times \frac{\left(z - \tilde{z}'_{mn}\right)}{\tilde{R}_{mn}^{3/2}}\,, \tag{10}$$

with $\tilde{R}_{mn} = \sqrt{\left(x - \tilde{x}'_{mn}\right)^2 + \left(z - \tilde{z}'_{mn}\right)^2}$, $\mathrm{Re}\left(\tilde{R}_{mn}\right) \geq 0$, representing the *complex distance* between the observer at $\mathbf{r} = (x, z)$ and the *complex source point* $\tilde{\mathbf{r}}'_{mn} = \left(\tilde{x}'_{mn}, \tilde{z}'_{mn}\right) = (mL_x + ib\sin\theta_n, ib\cos\theta_n)$. The tilde $\tilde{}$ identifies CSP-generated complex quantities, and the displacement parameter b (equal to the Fresnel length) is related to the beam lattice period L_x and the beam axis tilt angle θ_n via [6],

$$b = (L_x\cos\theta_n)^2/\lambda_0 \ll \tilde{R}_{mn}\,, \qquad \theta_n = \sin^{-1}(n\lambda_0/L_x)\,. \tag{11}$$

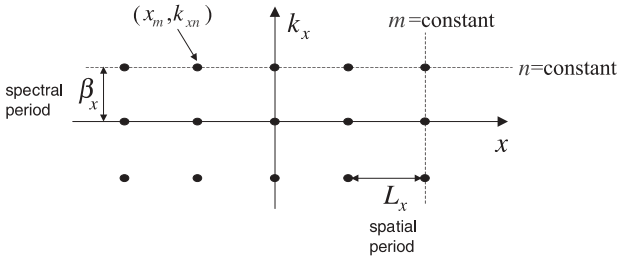

Fig. 2. Discretized Gabor phase space lattice. Spatial shift indexes m identify Gaussian beam (GB) launch points $x_m = mL_x$, $m = 0, \pm 1, \ldots$ Spectral shift indexes n identify linearly-phased GB tilts at $k_{xn} = n\beta_x$, $n = 0, \pm 1, \ldots$ Self-consistency condition: $L_x\beta_x = 2\pi$.

The Gabor GBs propagate when $|n| < L_x/\lambda_0$ (θ_n real) but decay away from the aperture when $|n| > L_x/\lambda_0$ (θ_n complex). For nontilted ($n = 0$) *narrow-waisted* (NW) beams ($L_x \lesssim \lambda_0 \ll d$), the Gabor coefficients A_{mn} in (9), which may be evaluated exactly by time-consuming integration [3, 4], can be *estimated* effectively in the NW-GB "far zone" away from the aperture by *sampling* the *aperture field distribution* $F(x)$ at the lattice points $x_m = mL_x$ [6, 7],

$$A_{mn} \approx \begin{cases} \left(L_x/\sqrt{2}\right)^{1/2} F(x_m), & n = 0\,, \\ 0, & n \neq 0\,. \end{cases} \tag{12}$$

The tilted ($n \neq 0$) beams, which here generate *evanescent* "far fields" away from the aperture (complex θ_n in (11)), are ignored. The waist of the propagating NW-CSP beams in the aperture plane is approximately equal to L_x. Since the CSP paraxial far zone approximation (10) can be invoked at moderate distance, the NW beam *superposition* can furnish accurate results even in the *near zone* of the *aperture*.

As shown in [8], more effective implementations can be obtained through the use of *propagation-matched* NW-beams. For instance, in the presence of a linearly phased aperture,

$$F(x) = g(x)\exp\left(ik_0 x\sin\theta_A\right), \tag{13}$$

where $g(x)$ is a real function and θ_A denotes a (real) tilt angle (Fig. 1), a more effective NW-GB discretization is given by (see [8] for details)

$$E_y(\mathbf{r}) \approx \sum_{|m| \leq (d/2L_x)} C_m \tilde{\mathcal{B}}_m(\mathbf{r}), \tag{14}$$

where, for simplicity, the subscript "$_{m0}$" is replaced by "$_m$", and

$$C_m = \left(L_x/\sqrt{2}\right)^{1/2} g(x_m), \quad |m| \leq (d/2L_x)\,, \tag{15}$$

$$\tilde{\mathcal{B}}_m(\mathbf{r}) = -ik_0 2^{5/4}\left(\frac{L_x}{8\pi k_0}\right)^{1/2} \exp\left(i\pi/4\right) \times \exp\left[ik_0\left(\tilde{R}_m + x_m\sin\theta_A + ib\right)\right] \times \frac{(z - ib\cos\theta_A)}{\tilde{R}_m^{3/2}}\,, \tag{16}$$

$$\tilde{R}_m = \sqrt{(x - x_m - ib\sin\theta_A)^2 + (z - ib\cos\theta_A)^2}\,, \qquad (17)$$

$$b = (L_x \cos\theta_A)^2/\lambda_0\,. \qquad (18)$$

The beam propagator in (16) differs from $\tilde{B}_{m0}$ in (10) by the phase shift $(ik_0 x_m \sin\theta_A)$ and by the different definitions of $\tilde{R}_m$ and b in (17), (18), respectively, which produce the propagation-matched tilt θ_A in the beam direction (see Fig. 1). For numerical validation of the above tilted beam synthesis, we consider the linearly phased distribution (13) with cosine tapering

$$g(x) = \begin{cases} \cos(\pi x/d), & |x| \le d/2\,, \\ 0, & |x| > d/2\,, \end{cases} \qquad (19)$$

with $\theta_A = 30^o$, and a fixed beam lattice period ($L_x = 0.1d$, i.e., ten beams). In Fig. 3, the near-zone field synthesized via (14) with a fixed number of NW tilted beams is compared with the reference solution (brute force Kirchhoff integration in (2)). The beam synthesis is hardly distinguishable from the reference solution. The stated number of beams in these simulations was arrived at via the pragmatic "scramblings" test, i.e., when the result remains insensitive to variations in the beam/lattice combinations, as noted in Sect. 1. Note that in order to achieve comparable accuracy using *nontilted* beams, about ten times as many such beams would be required.

2.1.2 Time domain

To perform the inversion from the frequency domain (FD) to the time domain (TD), we need both the ordinary and the analytic Fourier transforms (FTs) (see discussion in Sect. 1). The ordinary FT pair is given by

$$v(t) = \frac{1}{2\pi}\int_{-\infty}^{\infty} V(\omega)\exp(-i\omega t)d\omega\,,$$
$$V(\omega) = \int_{-\infty}^{\infty} v(t)\exp(i\omega t)dt\,, \qquad (20)$$

while the analytic FT $\overset{+}{v}(t)$ is given by

$$\overset{+}{v}(t) = \frac{1}{\pi}\int_{0}^{\infty} V(\omega)\exp(-i\omega t)d\omega, \quad \mathrm{Im}(t) \le 0\,, \qquad (21)$$

where $V(\omega)$ is the conventional FT of the real signal $v(t)$ (see (20)). The real signal for real t is recovered via

$$v(t) = \mathrm{Re}\left[\overset{+}{v}(t)\right]. \qquad (22)$$

Referring to Sect. 2.1.1 and Fig. 1, we now determine the TM-polarized incident field $e_y(\mathbf{r}, t)$ in the halfspace $z > 0$, generated by a linear-delay *pulsed* aperture field distribution $e_y(x, z = 0, t)$ of width d at $z = 0$, which corresponds to the Fourier-inverted frequency domain (FD) aperture field in (13), and has the form

$$e_y(x, z = 0, t) = \begin{cases} g(x)\,p(t - c_0^{-1} x\sin\theta_A), & |x| \le d/2\,, \\ 0, & |x| > d/2\,, \end{cases} \qquad (23)$$

where $p(t)$ is a pulse of length $T \ll d/c_0$, with c_0 representing the free-space wavespeed, $g(x)$ is the amplitude profile, and θ_A is the tilt angle (Fig. 1). The radiated field in $z > 0$ is obtained by Fourier inversion of the Kirchhoff integral in (2), weighted by the pulse spectrum $P(\omega)$ corresponding to $p(t)$. To obtain the Gabor PB expansion of the radiated TD field, the complex source point (CSP) high-frequency paraxial far zone FD NW-GB expansion in (14), weighted by the pulse spectrum $P(\omega)$, needs to be inverted to the TD. Recalling the effective treatment of linear phasing in Sect. 2.1.1, we use here linearly-phase-matched tilted beams (cf. (14)–(18)) instead of the nontilted beams in (10)–(12). We choose the Rayleigh (differentiated Gaussian) pulsed excitation,

$$p(t) = P_0 \frac{d^j}{dt^j}\exp\left[-\left(\frac{t - T/2}{\varsigma T}\right)^2\right], \qquad (24)$$

where P_0 is a normalization constant, and the variance ς is chosen so that the pulse width of $p(t)$ is $\sim T$. For this class of pulses, subject to constraints noted later on, the resulting TD analytic Fourier inversion integral can be

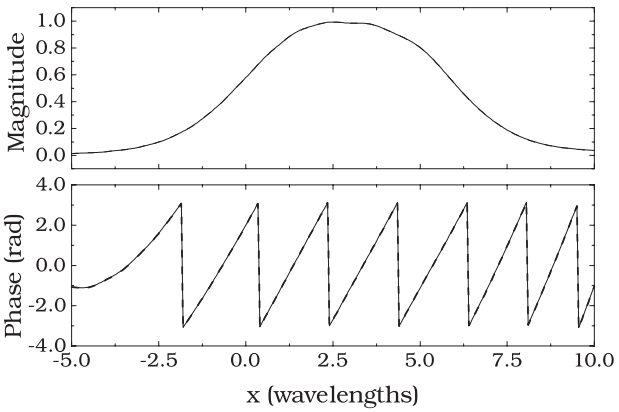

Fig. 3. Linearly phased cosine-tapered aperture distribution in (13), (19) ($d = 10\lambda_0, \theta_A = 30°$) (see Fig. 1). Near-zone ($z = 5\lambda_0$) radiated field synthesized via narrow-waisted tilted beams is compared with the reference solution (Kirchhoff integration in (2)). —— Reference solution; - - - Tilted beam synthesis ($L_x = 0.1d$, i.e., ten beams). Both solutions coincide on the scale of these plots.

approximated by rapidly computable *closed form* expressions. We found the following pulsed beam (PB) expansion for the radiated field excited by the aperture field in (23) (see [8,9] for details)

$$e_y(\mathbf{r},t) \sim \sum_{|m|\le(d/2L_x)} a_m b_m(\mathbf{r},t)\,,$$
$$\mathbf{r}=(x,z),\quad a_m=\left(\frac{L_x}{\sqrt{2}}\right)^{1/2} g(x_m)\,. \tag{25}$$

As in the FD, the TD Gabor expansion coefficients a_m in (25) have been approximated by sampling the profile function $g(x)$ in (23) at the lattice points $x_m = mL_x$. The PB propagator in (25) is given by

$$b_m(\mathbf{r},t) = \mathrm{Re}\left\{(-i)^j\beta_m\left[\mathcal{T}_m\Gamma\left(\frac{3+2j}{4}\right)\times \mathrm{M}_1^{(j)}\left(\frac{\bar t_m}{\mathcal{T}_m}\right) - 2i\bar t_m\Gamma\left(\frac{5+2j}{4}\right)\times\ \mathrm{M}_2^{(j)}\left(\frac{\bar t_m}{\mathcal{T}_m}\right)\right]\right\}\,, \tag{26}$$

where $\Gamma(\cdot)$ is the gamma function [2], and

$$\mathrm{M}_1^{(j)}(t) = {}_1\mathrm{F}_1\left(\frac{3+2j}{4},\frac{1}{2},-t^2\right)\,,$$
$$\mathrm{M}_2^{(j)}(t) = {}_1\mathrm{F}_1\left(\frac{5+2j}{4},\frac{3}{2},-t^2\right), \tag{27}$$

with ${}_1\mathrm{F}_1(\mu,\nu,t)$ denoting the Kummer confluent hypergeometric function [2]. The functions $\mathrm{M}_{1,2}^{(j)}$ can be computed efficiently using the rapidly converging expansions in [9]. Moreover,

$$\beta_m = 2^{j+1/2}\pi^{-1/2}(\mathcal{T}_m)^{-j-5/2}\Lambda_m P_0\varsigma T\,, \tag{28}$$

$$\bar t_m = t-\tau_m-T/2,\quad \mathcal{T}_m=\sqrt{T_m^2+\varsigma^2T^2}\,, \tag{29}$$

$$\tau_m = c_0^{-1}(R_m + x_m\sin\theta_A)\,, \tag{30}$$

$$T_m = \frac{L_x\cos\theta_A}{c_0}\left[\frac{2}{\pi}\left(1-\frac{z_{bm}}{R_m}\right)\right]^{1/2}\,, \tag{31}$$

$$\Lambda_m = -i2^{5/4}\sqrt{\frac{L_x}{8\pi c_0}z}R_m^{-3/2}\exp(i\pi/4)\,, \tag{32}$$

$$R_m=\sqrt{x_{bm}^2+z_{bm}^2}\,, \tag{33}$$

and (x_{bm}, z_{bm}) are beam-centered coordinates (Fig. 1),

$$\begin{bmatrix} x_{bm}\\ z_{bm}\end{bmatrix} = \begin{bmatrix}\cos\theta_A & -\sin\theta_A\\ \sin\theta_A & \cos\theta_A\end{bmatrix}\begin{bmatrix} x-x_m\\ z\end{bmatrix}\,. \tag{34}$$

The propagator in (26) is a Gaussian PB wavepacket, whose collimation is controlled by the discretization period L_x. The constraints arising from the various approximations employed in the analysis can be formalized in terms of a nondimensional critical estimator which contains certain relevant problem parameters (see [8,9] for details),

$$Q \equiv N_b^{-1}\sqrt{\frac{\kappa(\cos\theta_A)^3}{\chi}} \ll 1\,. \tag{35}$$

Here, the integer $N_b = d/L_x$ represents the number of beams in the expansion (25), $\kappa = \Omega T/2\pi$ (with Ω denoting the pulse effetive bandwidth), and $\chi = z/F_d$ is the distance to the observation plane scaled by the Fresnel distance of the aperture, $F_d = d^2/(c_0T)$. The nondimensional estimator Q in (35) shows how changes in one parameter can be compensated by corresponding changes in the other parameters so as to remain in the legitimized range. For example, at *larger* observation distances z, *fewer* beams are required.

For illustration of the performance of the NW-PB algorithm in (25), we show results for the TD counterpart of the cosine-tapered linearly phased FD aperture profile in (13) and (19). The exciting (fourth-order) Rayleigh pulse and its FD spectrum are shown in Fig. 4. The radiated field is shown and validated in the plots of Fig. 5, for test conditions which are detailed in the figure caption. The constraints pertaining to these results meet the nondimensional estimator criterion in (35). The reference solution used in these examples is a brute-force space-time Kirchhoff integration [8]. To better quantify the accu-

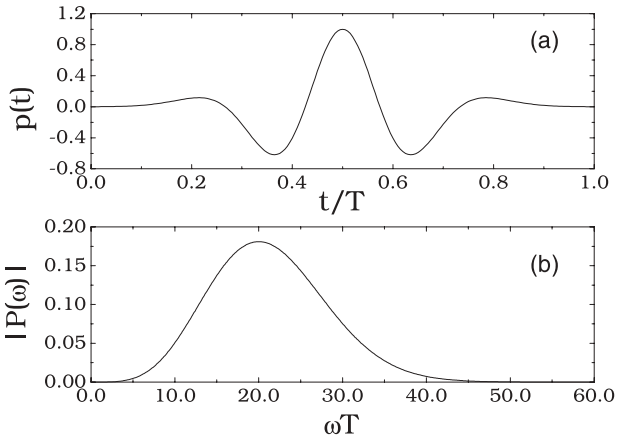

Fig. 4. Fourth-order Rayleigh pulse. (a): Temporal profile in (24). (b): Spectrum (magnitude). Parameters: $j=4$, $P_0 = T^4/30\,000$, $\varsigma = 1/\sqrt{50}$.

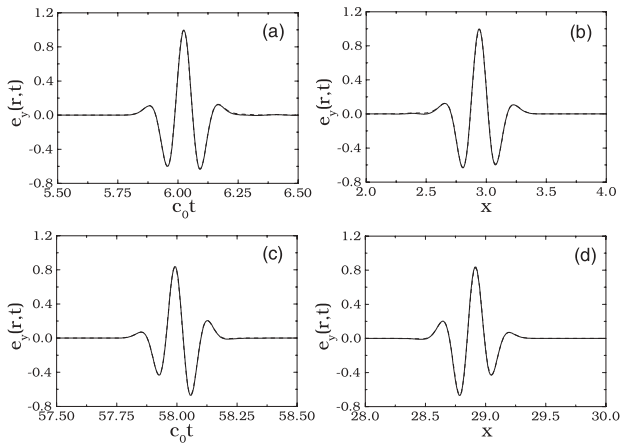

Fig. 5. Radiated field due to the pulsed linear-delay ($\theta_A = 30°$) cosine-tapered aperture distribution in Fig. 4. Parameters: $c_0T = 0.5$, $d = 5 = 10c_0T$ (arbitrary units). Observation points for the temporal profiles are located on the tilted beam axis θ_A. (a): Temporal profile at $x = 2.89$, $z = 5 = 0.1F_d$ (arbitrary units), 25 beams ($Q = 0.26$, $\Delta e_y = -32$ dB; see (35), (36)); (b): Spatial transverse profile at $z = 5$, $c_0t = 6.05$, 25 beams ($Q = 0.26$); (c): Temporal profile at $x = 28.9$, $z = 50 = F_d$, 8 beams ($Q = 0.25$, $\Delta e_y = -33$ dB); (d): Spatial transverse profile at $z = 50$, $c_0t = 58$, 8 beams ($Q = 0.25$). Reference solutions (solid curves) and beam solutions (dashed curves) coincide on the scale of the plots.

racy of the NW-PB approach, we have computed the r.m.s. error

$$\Delta e_y = \frac{\int_{-\infty}^{\infty} \left| e_y^{(ref)} - e_y^{(beam)} \right|^2 dt}{\left[\int_{-\infty}^{\infty} \left| e_y^{(ref)} \right|^2 dt \int_{-\infty}^{\infty} \left| e_y^{(beam)} \right|^2 dt \right]^{1/2}} \qquad (36)$$

at various observation points **r**; values are displayed in the Fig. 5 caption (note the pulse distortion, due to near-zone/far-zone transition, at the Fresnel length F_d). Quantitatively, values of $Q \approx 0.3$ (see (35)) were found to yield r.m.s. errors $\Delta e_y < -30$ dB.

2.2 Transmission/reflection due to layered dielectrics

Prototype studies have been conducted in the FD for plane [6] and circular cylindrical [7] dielectric layers, and in the TD for plane layers [9]. Because there are no results so far for TD excitation of a cylindrical layer, our presentation here deals only with the planar case. The problem geometry is shown in Fig. 6. An infinite plane weakly dispersive dielectric layer with lower interface at $z = z_L$ has thickness d_1, relative permittivity ϵ_{r1}, and electrical conductivity σ_1. Both ϵ_{r1} and σ_1 are assumed to be frequency independent, and attention is restricted to slightly lossy layers, i.e., $\sigma_1/(\omega\epsilon_0\epsilon_{r1}) \ll 1$.

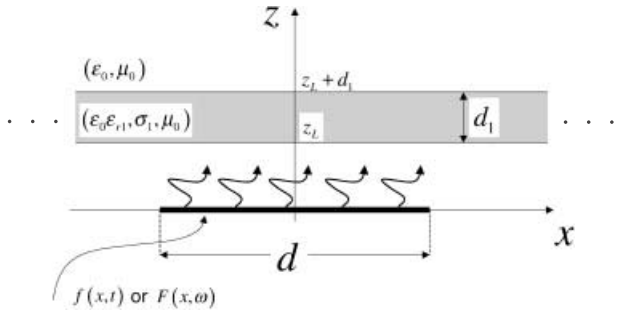

Fig. 6. Problem geometry pertaining to Sect. 2.2: a large truncated aperture field distribution of width d, with space-time dependence $f(x,t)$ and temporal spectrum $F(x,\omega)$, radiates in the presence of a homogeneous weakly dispersive dielectric layer of thickness d_1, with relative dielectric permittivity ϵ_{r1} and electrical conductivity σ_1. The field is observed in the half-space $z > z_L + d_1$. The numerical simulations in Sect. 2.2.2 have been carried out for $z_L = 0$.

2.2.1 Frequency domain

As stated in Sect. 1, the layer-transmitted/reflected fields excited by the NW-GB-discretized incident field in (9) are obtained by efficient quasi-real ray tracing implemented through paraxial beam shooting. Basically, a single multihop GB is tracked along its real-ray axis via conventional real ray tracing; the slightly complex NW-GB spectrum of the emerging GB is accounted for approximately through augmentation of its on-axis (real ray) value by a complex phase correction in the perpendicular distance from the axis to the off-axis observer [6]. The reader is referred to [6] for validation, calibration and performance assessment of the algorithm pertaining to the fields excited by linearly and quadratically phased (focusing) aperture field distributions; transmission of the latter through the layer poses a problem of substantial complexity. In [9], a slightly different, though similar in spirit, FD approximation was developed, which facilitates subsequent analytic Fourier inversion to the TD (see Sect. 2.2.2). We consider aperture field distributions

$$\begin{aligned} F(x,\omega) &= g(x)\exp\left[ik_0\phi(x)\right], \\ \phi(x) &= x\sin\theta_A + \phi_{NL}(x), \end{aligned} \qquad (37)$$

where $g(x)$ is a spatial tapering function, and $\phi(x)$ is a general nonlinear phase function, which is conveniently split into a linear part $x\sin\theta_A$ (θ_A real) plus a nonlinear remainder $\phi_{NL}(x)$. Also in this case, we use linearly-phase-matched tilted beams (cf. (14)–(18)) to parameterize the linear phasing more effectively. Referring to [9] for details, the y-directed layer-transmitted field E_y^t in the half-space $z > z_L + d_1$ is discretized approximately in terms of tilted NW-GBs as

$$\begin{aligned} E_y^t(\mathbf{r}) \sim{}& \left(1 - \mathcal{R}_{1A}^2\right) \\ &\times \sum_{|m| \le d/(2L_x)} A_m \sum_{q=0}^{N_q} \mathcal{R}_{1A}^{2q} \tilde{\mathcal{B}}_m^{(q)}(\mathbf{r}), \end{aligned} \qquad (38)$$

where $\mathbf{r} = (x, z)$, $\tilde{\mathcal{B}}_m^{(q)}$ are the GB propagators, and the (Gabor) expansion coefficients A_m are obtained approximately as in (12), i.e., by sampling the phased aperture field distribution at the Gabor lattice points,

$$\begin{aligned} A_m &\sim \left(L_x/\sqrt{2}\right)^{1/2} F(x_m) \exp(-ik_0 x_m \sin\theta_A) \\ &= \left(L_x/\sqrt{2}\right)^{1/2} g(x_m) \exp\left[ik_0 \phi_{NL}(x_m)\right], \\ &\quad |m| \le (d/2L_x)\,. \end{aligned} \tag{39}$$

In (38), $\mathcal{R}_{1A}$ represents the plane-wave TM Fresnel reflection coefficient

$$\mathcal{R}_{1A} = \frac{\cos\theta_A - \sqrt{\epsilon_{r1} - \sin^2\theta_A}}{\cos\theta_A + \sqrt{\epsilon_{r1} - \sin^2\theta_A}}\,, \tag{40}$$

and the q-index tags *roundtrip* reflections inside the dielectric layer (i.e., $2q$ *individual* reflections at each layer interface), with N_q denoting the total number of roundtrips retained. Apart from the explicit internal roundtrip reflection coefficient factor $\mathcal{R}_{1A}^{2q}$ in (38), the GB propagator represents the wavefield contribution, at the observer, due to the m-th basis GB, after undergoing q internal roundtrip reflections, and is given by [9]

$$\begin{aligned} \tilde{\mathcal{B}}_m^{(q)}(\mathbf{r}) \sim\ & -i2^{5/4}\left(z - \tilde{z}_{fq}\right)\sqrt{\frac{k_0 L_x}{8\pi \tilde{R}_{fmq}^3}} \\ & \times \exp\left[i\left(k_0\tilde{\psi}_{mq} + \pi/4\right)\right], \end{aligned} \tag{41}$$

where

$$\begin{aligned} \tilde{\psi}_{mq} &= \tilde{R}_{fmq} + x_m \sin\theta_A + ib \\ &\quad + \frac{(1+2q)\left(\epsilon_{r1}^{(e)}\cos^2\theta_t - \cos^2\theta_A\right) d_1}{\sqrt{\epsilon_{r1}^{(e)}}\cos^3\theta_t}\,, \end{aligned} \tag{42}$$

$$\epsilon_{r1}^{(e)} = \epsilon_{r1} + i\frac{\sigma_1}{\omega\epsilon_0}\,, \tag{43}$$

and $\tilde{R}_{fmq}$ represents the *complex distance* between the observation point at (x, z) and the *complex virtual focus* $\tilde{\mathbf{r}}_{fmq} \equiv \left(\tilde{x}_{fmq}, \tilde{z}_{fq}\right)$ (see Fig. 7),

$$\begin{aligned} \tilde{R}_{fmq} &= \sqrt{(x - \tilde{x}_{fmq})^2 + (z - \tilde{z}_{fq})^2}, \\ &\mathrm{Re}(\tilde{R}_{fmq}) \ge 0\,, \end{aligned} \tag{44}$$

$$\begin{aligned} \tilde{x}_{fmq} &= x_m + ib\sin\theta_A + \frac{(1+2q)d_1}{\sqrt{\epsilon_{r1}^{(e)}}\cos^3\theta_t} \\ &\cdot \left(\sqrt{\epsilon_{r1}^{(e)}}\sin\theta_t\cos^2\theta_t - \sin\theta_A\cos^2\theta_A\right), \end{aligned} \tag{45}$$

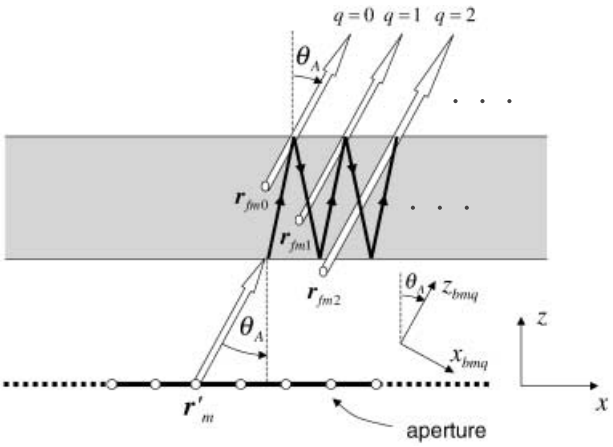

Fig. 7. Schematic interpretation of the *quasi-real* ray-tracing scheme pertaining to transmission of a single NW-CSP beam through the layer (cf. (41)). A *complex ray* is traced from the CSP at $\tilde{\mathbf{r}}'_m$ along a *complex* trajectory to the intersection of the *real* beam axis with the *real* layer (lower) interface; the path into the layer proceeds entirely in *real* space along the beam axis, undergoing q roundtrip reflections inside the dielectric layer. The last segment, which reaches the observer, proceeds in *complex* space as a *complex ray* emanating from the complex virtual focus $\tilde{\mathbf{r}}_{fmq}$. In real configuration space, these complex rays describe NW paraxial Gaussian beams. White arrows denote complex rays; black arrows denote real rays; "$\circ$" denotes the locations of the complex source points $\tilde{\mathbf{r}}'_m$ and the complex virtual foci $\tilde{\mathbf{r}}_{fmq} \equiv (\tilde{x}_{fmq}, \tilde{z}_{fq})$ in (45) and (46). The beam coordinates (x_{bmq}, z_{bmq}) are sketched in the inset.

$$\tilde{z}_{fq} = d_1 + ib\cos\theta_A - \frac{(1+2q)d_1\cos^3\theta_A}{\sqrt{\epsilon_{r1}^{(e)}}\cos^3\theta_t}\,. \tag{46}$$

In (41)–(46), the transmission angle θ_t is related to θ_A via Snell's law, whereas b is the GB-CSP displacement parameter (Fresnel length) in (18). Referring to Fig. 7, the approximation in (41)–(46) corresponds to tracing a ray along a *complex* trajectory (white arrow) from the CSP at $\tilde{\mathbf{r}}'_m$ to the intersection of the *real* beam axis with the *real* layer (lower) interface; from there, the path into the layer proceeds entirely in *real* configuration space, along the beam axis, undergoing q roundtrip reflections between the layer boundaries (black arrows). The last segment, which reaches the observer, proceeds in *complex* space, as a *complex ray* (white arrows) emanating from the complex virtual focus $\tilde{\mathbf{r}}_{fmq}$. In real configuration space, these complex rays describe NW paraxial GBs. The results in (38)–(46) set the stage for the analytic TD inversion described below.

2.2.2 Time domain

The desired transient y-directed electric field $e_y^t(\mathbf{r}, t)$ transmitted through the planar dielectric layer in Fig. 6 is excited by the TM-polarized aperture field $e_y^i(x, z = 0, t)$ as in (23), with space-time distribution $f(x, t)$ (which

is the Fourier inversion of the FD distribution in (37) weighted by the spectrum $P(\omega)$ of the pulse $p(t)$ (see Sect. 2.1.2)),

$$f(x,t) = g(x)\, p\left[t - c_0^{-1}\phi(x)\right], \tag{47}$$

with $\phi(x)$ defined in (37). The PB synthesis of the layer-transmitted wavefield $e_y^t(\mathbf{r},t)$ into the halfspace $z > z_L + d_1$ is obtained via analytic Fourier inversion (cf. (21) and (22)) of the corresponding Gabor-based FD-GB synthesis in (38) [9],

$$e_y^t(\mathbf{r},t) \sim \left(1-\bar{\mathcal{R}}_{1A}^2\right) \cdot \sum_{|m|\le(d/2L_x)} a_m \sum_{q=0}^{N_q} \bar{\mathcal{R}}_{1A}^{2q} b_m^{(q)}(\mathbf{r}, t-t_m), \tag{48}$$

where $\mathbf{r} = (x,z)$, and $b_m^{(q)}$ are the PB propagators weighted by the plane-wave TM Fresnel reflection coefficients in (40); the amplitude coefficients a_m and time delays t_m are obtained by sampling the aperture field distribution amplitude and nonlinear phasing, respectively, in (47) at the lattice points $x_m = mL_x$,

$$a_m = \left(L_x/\sqrt{2}\right)^{1/2} g(x_m), \quad t_m = \phi_{NL}(x_m)/c_0\,. \tag{49}$$

For Rayleigh pulses as in (24) and slight losses, following the same procedure as in Sect. 2.1.2, one obtains a closed-form expression for the PB propagators $b_m^{(q)}$ formally analogous to that in (26) [9]

$$b_m^{(q)}(\mathbf{r},t) = \mathrm{Re}\left\{(-i)^j \beta_{mq}\left[\mathcal{T}_{mq}\Gamma\left(\frac{3+2j}{4}\right) \times \mathrm{M}_1^{(j)}\left(\frac{\bar{t}_{mq}}{\mathcal{T}_{mq}}\right) - 2i\bar{t}_{mq}\Gamma\left(\frac{5+2j}{4}\right) \times \mathrm{M}_2^{(j)}\left(\frac{\bar{t}_{mq}}{\mathcal{T}_{mq}}\right)\right]\right\}, \tag{50}$$

with the special functions $\mathrm{M}_{1,2}^{(j)}$ defined in (27). Moreover,

$$\beta_{mq} = 2^{j+1/2}\pi^{-1/2}(\mathcal{T}_{mq})^{-j-5/2}\Lambda_{mq} P_0 \varsigma T\,, \tag{51}$$

$$\bar{t}_{mq} = t - \tau_{mq} - T/2, \quad \mathcal{T}_{mq} = \sqrt{T_{mq}^2 + \varsigma^2 T^2}\,, \tag{52}$$

$$\tau_{mq} = c_0^{-1}\left[R_{fmq} + x_m \sin\theta_A + \frac{(1+2q)\left(\epsilon_{r1}\cos^2\theta_t - \cos^2\theta_A\right) d_1}{\sqrt{\epsilon_{r1}}\cos^3\theta_t}\right], \tag{53}$$

$$T_{mq} = \frac{L_x\cos\theta_A}{c_0}\left[\frac{2}{\pi}\left(1 - \frac{z_{bmq}}{R_{fmq}}\right)\right]^{1/2}, \tag{54}$$

$$\Lambda_{mq} = -i2^{5/4}\sqrt{\frac{L_x}{8\pi c_0}}(z - z_{fq})\, R_{fmq}^{-3/2} \times \exp(-\kappa_1 R_{Lq} + i\pi/4)\,, \tag{55}$$

$$\kappa_1 = \frac{\sigma_1}{2c_1\epsilon_0\epsilon_{r1}}, \quad R_{Lq} = (1+2q)d_1/\cos\theta_t\,, \tag{56}$$

$$\theta_t = \sin^{-1}\left(\sin\theta_A/\sqrt{\epsilon_{r1}}\right), \tag{57}$$

$$R_{fmq} = \sqrt{(x - x_{fmq})^2 + (z - z_{fq})^2}\,, \tag{58}$$

$$x_{fmq} = x_m + \frac{(1+2q)d_1}{\sqrt{\epsilon_{r1}}\cos^3\theta_t} \times \left(\sqrt{\epsilon_{r1}}\sin\theta_t\cos^2\theta_t - \sin\theta_A\cos^2\theta_A\right), \tag{59}$$

$$z_{fq} = d_1 - \frac{(1+2q)d_1\cos^3\theta_A}{\sqrt{\epsilon_{r1}}\cos^3\theta_t}\,. \tag{60}$$

In (56), $c_1 = c_0/\sqrt{\epsilon_{r1}}$ denotes the wavespeed in the dielectric layer. As for the free-space propagation, it is possible to formalize certain constraints arising from the various approximations in terms of a nondimensional estimator, which is formally identical to that in (35) with $\chi = (z - d_1)/F_d$, (see [9] for details).

We have selected the example in Fig. 8, involving a Gaussian-tapered aperture field distribution with linear and quadratic delay

$$g(x) = \exp\left(-\alpha x^2/d^2\right), \quad \phi(x) = x\sin\theta_A - \beta x^2, \quad \beta > 0\,, \tag{61}$$

which generates a tilted *focusing* Gaussian beam; the parameter α is chosen such that the initial distribution tapers to zero for $|x| > d/2$, with $L_f = d_1 + 1/(2\beta)$ denoting the distance from the aperture to the location of substantial focusing (focal plane) of the layer-transmitted field. The problem parameters are listed in the figure caption. The reference solution is based on brute-force integration of the exact FD spectral (plane wave) representation and use of the inverse fast Fourier transform (FFT) (see [9]). In Fig. 8a, the comparison between the PB synthesis and the reference solution at a fixed observation point on the focal plane shows excellent agreement. Note the pulse distortion during passage through the focal plane (see also Fig. 5c). The convergence, in terms of the normalized r.m.s. error Δe_y (cf. (36)), with respect to Q in (35) and the number of internal roundtrip reflections N_q is illustrated in Figs. 8b and 8c, respectively. In [9, 10], results are presented and discussed from an extensive series of numerical simulations, involving various aperture field distributions and parameter combinations. Overall,

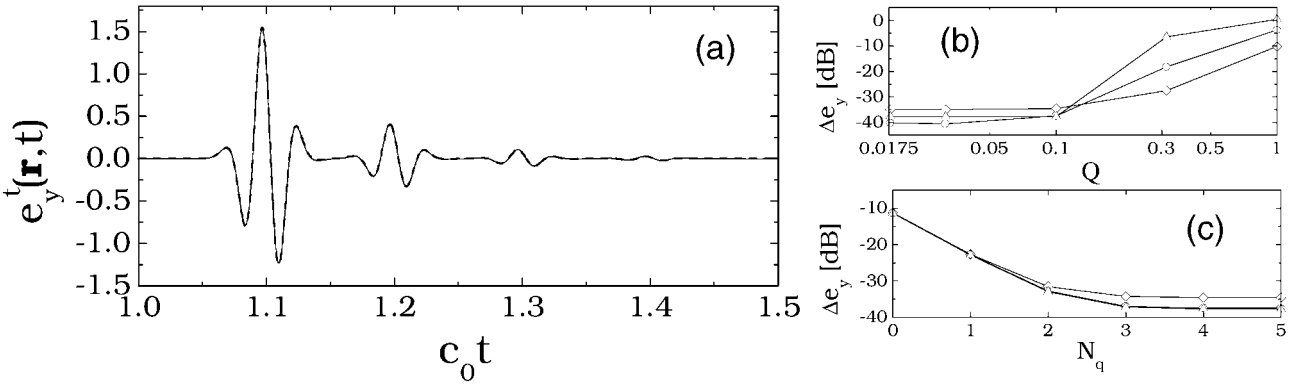

Fig. 8. Geometry as in Fig. 6, with $d = 1$ (arbitrary units), $c_0 T = 0.1d$, $z_L = 0$, $d_1 = 0.5 c_1 T$, $\epsilon_{r1} = 10$, $\sigma_1 = 0.01\,\mathrm{S/m}$. Gaussian-tapered quadratic delay aperture field distribution in (61), with $\alpha = 20$, $\theta_A = 0$ (nontilted), and $\beta = 0.5$ (focal plane at $L_f = d_1 + 1$). Fourth-order Rayleigh pulsed excitation as in Fig. 4. (a): Comparison between PB synthesis and reference solution for transmitted field at a fixed observation point on the focal plane ($x = 0, z = d_1 + 1$). —— Reference solution; - - - PB synthesis with $N_b = 80$ ($Q = 0.1$) and $N_q = 3$. Reference solution and PB synthesis coincide on the scale of the plot. (b), (c): r.m.s. error vs. Q (at $N_q = 3$) and vs. N_q (at $Q = 0.1$), respectively, for $x = 0$ and various observation distances. —◇— $z = d_1 + 0.25$; —○— $z = d_1 + 2$; —△— $z = d_1 + 10$. N_q =no. of internal roundtrip reflections.

accurate and robust predictions were observed within the range $Q < 0.1$ (consistent with the results in Sect. 2.1.2) and with N_q chosen such that the magnitude of the first omitted term is less than 0.1% of that of the leading term.

2.3 Transmission/reflection due to moderately rough dielectric interfaces

Treating wave interaction with a (moderately) rough dielectric interface (which is a complex noncanonical geometry) by the NW-GB algorithm poses a challenging test. The problem geometry is shown in Fig. 9. A TM-polarized FD or TD incident field generated by a linearly phased aperture field distribution of width d at $z = z_A$ is assumed to impinge from free-space onto a homogeneous slightly lossy dielectric halfspace of relative permittivity ϵ_{r1} and electrical conductivity $\sigma_1 \ll \omega\epsilon_0\epsilon_{r1}$, bounded by a moderately rough interface described by the continuous function $h(x)$. Due to space limitations, we present only the main results for the scattered field, omitting technical details which can be found in [11].

2.3.1 Frequency domain

The incident field E_y^i being considered is the same as in (1) and (2), but now emanating from an aperture field distribution at $z = z_A$ and propagating along the negative z-axis. Invoking the NW-GB discretization for the incident field as in (9)–(12) reduces the reflected field determination to tracking each incident GB through reflection from the interface and recombining them at the observer. In [12], such an approach was pursued by extending the quasi-real ray tracing (beam shooting) algorithms in [6, 7] and Sect. 2.2.1. Accurate and robust predictions were obtained with modest computing times and resources (see [12] for details). Subsequently, an alternative FD approach was developed [11], based on Kirchhoff physical optics (PO) approximations, whose inversion to the TD, via the algorithm in [8] and Sect. 2.1.2, was found to be particularly convenient. In this section, we briefly review the FD PO formulation and its Gabor-based NW-GB beam discretization. The interface is assumed to be located in the collimation zone of the aperture so that the incident field can be approximated by a truncated tapered plane wave (see Fig. 9),

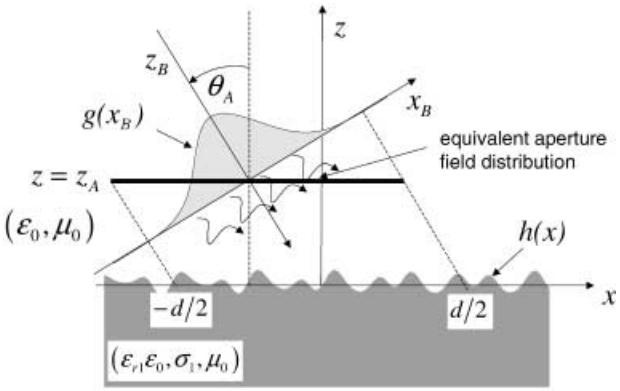

Fig. 9. Problem geometry pertaining to Sects. 2.3 and 2.4. An aperture-generated FD or TD TM-polarized quasi-plane-wave wavefield impinges from free space onto a dielectric halfspace with relative permittivity ϵ_{r1} and conductivity σ_1, bounded by a moderately rough interface $z = h(x)$.

$$E_y^i(\mathbf{r}, \omega) \sim g(x_B) \exp(ik_0 z_B)\,, \tag{62}$$

with (x_B, z_B) denoting the beam coordinates in Fig. 9. In the asymptotic high-frequency range, and for smooth roughness on the wavelength scale, the reflected field is

approximated by the Kirchhoff PO integral

$$E_y^r(\mathbf{r},\omega) \sim -\int_{C_{PO}} J_{PO}^r(x',\omega) \times \frac{\partial}{\partial\zeta} G_{2D}(\mathbf{r};\mathbf{r}_h';k_0)\,d\ell' \,, \tag{63}$$

where $\mathbf{r}=(x,z)$, $\mathbf{r}_h' \equiv (x',h(x'))$, C_{PO} extends over the illuminated portion of the 1-D surface $z=h(x)$, G_{2D} is the 2-D free-space Green's function in (3), $d\ell'$ is the incremental arc-length measured along the surface tangent, and $\partial/\partial\zeta$ denotes the normal derivative. The incident field tapering is chosen so that the illuminated portion of the interface, C_{PO}, is essentially confined to the interval $|x| \le d/2$. The PO equivalent magnetic surface current density J_{PO}^r is given by twice the tangential reflected electric field at the interface, obtained from the canonical solution of infinite plane-wave scattering by a plane dielectric boundary locally tangent to the rough surface profile

$$J_{PO}^r(x,\omega) = 2\mathcal{R}(x,\omega)E_y^i(x,h(x),\omega) \,, \tag{64}$$

with $\mathcal{R}$ denoting the *local* TM plane-wave Fresnel reflection coefficient (see [11] for details). The FD PO integral in (63) is formally analogous to the FD Kirchhoff aperture radiation integrals in (2). The only major difference is that the line integration in (63) is performed along the 1-D rough surface profile $z=h(x)$ instead of a 1-D planar aperture as in (2). With this observation, in [11], a NW-GB expansion was obtained for the PO reflected field in terms of propagation-matched tilted beams,

$$E_y^r(\mathbf{r}) \sim \sum_{|m|\le(d/2L_x)} C_m^r \tilde{\mathcal{B}}_m^r(\mathbf{r}) \,. \tag{65}$$

In (65), the coefficients C_m^r are approximated by sampling the PO equivalent current J_{PO}^r at the Gabor lattice points $x_m = mL_x$; these coefficients depend on the incident field and on the local properties of the surface. The NW-GB propagators $\tilde{\mathcal{B}}_m^r$ are formally analogous to those in (14), and propagate along the local reflection direction according to Snell's law. The transmitted field is obtained in a similar manner. The reader is referred to [11] for theoretical and implementation details.

2.3.2 Time domain

Again exploiting the formal analogy between the reflected NW-GB propagators $\tilde{\mathcal{B}}_m^r$ and those in (14), the TD inversion of the FD reflected field NW-GB expansion in (65) is straightforward, proceding along the guidelines in Sect. 2.1.2. Thus, for pulsed quasi-plane-wave incidence,

$$e_y^i(\mathbf{r},t) \sim g(x_B)\,p\big(t-c_0^{-1}z_B\big) \,, \tag{66}$$

with $p(t)$ being a Rayleigh pulse as in (24), one obtains the following NW-PB expansion for the reflected field

$$e_y^r(\mathbf{r},t) \sim \sum_{|m|\le(d/2L_x)} c_m^r b_m^r(\mathbf{r},t-t_m) \,. \tag{67}$$

Theoretical and implementation details, as well as the corresponding expansion for the transmitted field, can be found in [11]. We note that the Gabor expansion coefficients c_m^r and the time delay t_m are dependent on the incident field and on local properties of the surface, while the NW-PB propagators b_m^r are formally analogous to those in (26), with propagation direction matched to the local reflection direction.

In order to validate and calibrate the algorithm, we developed an independent moment-method-based full-wave reference solution (see [11] for details). Typical results are shown in Fig. 10. Specifically, for the temporal behavior of the scattered field at a fixed observation point in the presence of the interface profile in Fig. 10a, Fig. 10b shows the comparison between the reference solution and the NW-PB synthesis (150 beams) in (25), which involves a modest computational effort when compared with conventional Kirchhoff-PO integration. Good agreement is observed even in the finer details, with a r.m.s. error $\Delta e_y = -30$ dB. Similar results have been obtained for the transmitted field. Convergence and accuracy issues are discussed in [11]. Concerning the range of applicability, we have found fairly accurate predictions $\big(\Delta e_y \lesssim -20\,\mathrm{dB}\big)$ for roughness with maximum height $h_{max} \lesssim 0.5c_0T$, (average) curvature radii $\bar{r}_c \gtrsim 2c_0T$ and maximum slopes $\alpha_{max} \lesssim 40°$, for nearly-

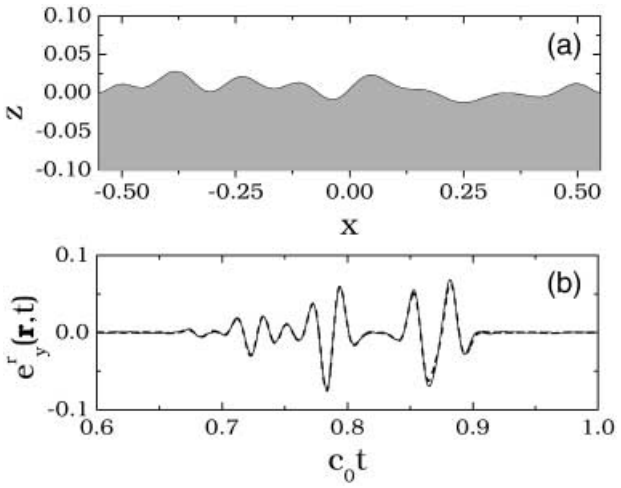

Fig. 10. Simulation geometry and parameters for rough surface scattering. (a): Rough surface profile (arbitrary units). (b): Temporal behavior of reflected field at $x=-0.4$, $z=0.5$. Aperture tapering: $f(x)=\exp\big(-18x^2/(\pi d^2)\big)$, $d=1$. Fourth-order Rayleigh pulsed excitation as in Fig. 4. Simulation parameters: $\epsilon_{r1}=4.5$, $\sigma_1 = 0.012\,\mathrm{S/m}$, $z_A=0.2$, $\theta_A=0$, $c_0T=0.08$. —— Reference solution; - - - NW-PB synthesis (150 beams). r.m.s. error: $\Delta e_y = -30$ dB.

vertical incidence $\left(\theta_A \lesssim 30^\circ\right)$ and for dielectrics with $\sigma_1/(\Omega\epsilon_0\epsilon_{r1}) \lesssim 0.05$.

2.4 Scattering by objects embedded below moderately rough dielectric interfaces

We again refer to the problem geometry in Fig. 9, but now include a buried target with relative permittivity ϵ_{r2} and electric conductivity $\sigma_2 \approx 0$ occupying a region $\mathcal{D}$ in the dielectric halfspace (see Fig. 11). Our interest lies in computing the target-scattered field observed at $\mathbf{r} = (x, z)$ above the interface. These results will be used subsequently (Sect. 3) in inverse scattering scenarios.

2.4.1 Frequency domain

The $y-$directed FD *total* field observed in free space can be written as

$$E_y(\mathbf{r}, \omega) = E_y^b(\mathbf{r}, \omega) + E_y^s(\mathbf{r}, \omega)\,, \tag{68}$$

where E_y^b represents the *background field* (i.e., the field in the absence of the target), and

$$E_y^s(\mathbf{r}, \omega) = \frac{\omega^2}{c_0^2} \iint\limits_{\mathcal{D}} E_y(\mathbf{r}', \omega) G_b(\mathbf{r}, \mathbf{r}', \omega) \times O(\mathbf{r}', \omega) d\mathbf{r}'\,, \tag{69}$$

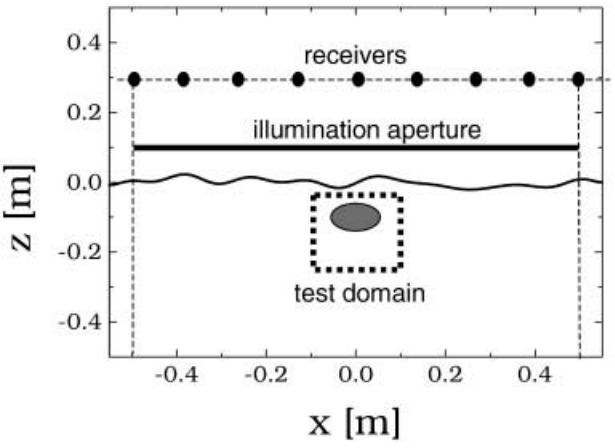

Fig. 11. Simulation geometry and parameters for forward and inverse scattering of objects embedded below moderately rough interfaces. An elliptic (10 cm × 6 cm) dielectric target with $\epsilon_{r2} = 3.5$ and $\sigma_2 = 0$ is buried with center at 10 cm below the nominal ground ($z = 0$). The rough surface profile realization was randomly generated so as to simulate typical moderate roughness (maximum-to-minimum height ∼ 4 cm, maximum slope ∼ 32°) for a class of realistic soils ($\epsilon_{r1} = 4$, $\sigma_1 = 0.01$ S/m). The reflected field is sampled at $N_r = 11$ receivers located at $z^r = 0.3$ m and $x^r = -0.5$ m, -0.4 m, ..., 0.5 m. Incident field tapering $g(x) = \cos(\pi x/d)$. Parameters: $d = 1$ m, $\theta_A = 0$, $z_A = 0.1$ m. Fourth-order Rayleigh pulsed excitation as in Fig. 4 ($T \sim 1.3$ ns).

is the field scattered by the target. In (69), G_b represents the FD Green's function of the rough-interface dielectric halfspace, E_y is the *total* field in the target region, and

$$O(\mathbf{r}', \omega) = \left[\epsilon_r(\mathbf{r}') - \epsilon_{r1}\right] + i\frac{\left[\sigma(\mathbf{r}') - \sigma_1\right]}{\omega\epsilon_0} = \Delta\epsilon_r(\mathbf{r}') + i\frac{\Delta\sigma(\mathbf{r}')}{\omega\epsilon_0} \tag{70}$$

is referred to as the *object function*. The integration in (69) is limited to the region $\mathcal{D}$ in which the object function is nonzero. In the presence of low-contrast targets ($|\Delta\epsilon_r|/\epsilon_{r1} \ll 1$), we can use the linearizing Born approximation [13] which replaces the total field E_y inside the target by the transmitted field E_y^t in $\mathcal{D}$ in the absence of the target, yielding

$$E_y^s(\mathbf{r}, \omega) \approx k_0^2 \iint\limits_{\mathcal{D}} \Delta\epsilon_r(\mathbf{r}') E_y^t(\mathbf{r}', \omega) \times G_b(\mathbf{r}, \mathbf{r}', \omega) d\mathbf{r}'\,, \tag{71}$$

where the (weak) conductivity contrast contribution $\Delta\sigma$ in (70) has also been neglected. For justification and other approaches, see [14–16]. The unperturbed transmitted field E_y^t and the Green's function G_b in (71), which account for distortion of the useful signal due to the twice-traversed rough air-ground interface, are computed efficiently via the PO-GB syntheses detailed in [11, 17], which are conceptually analogous to that in (65). We shall not consider the FD formulation further because our eventual application is for pulsed excitation.

2.4.2 Time domain

For pulsed excitation, with time dependence $p(t)$, by Fourier inversion of (68) and (71), one obtains

$$e_y(\mathbf{r}, t) = e_y^b(\mathbf{r}, t) + e_y^s(\mathbf{r}, t)\,, \tag{72}$$

$$e_y^s(\mathbf{r}, t) \approx \iint\limits_{\mathcal{D}} \Delta\epsilon_r(\mathbf{r}') \bar{u}(\mathbf{r}, \mathbf{r}', t) d\mathbf{r}'\,, \tag{73}$$

where the Born TD kernel $\bar{u}(\mathbf{r}, \mathbf{r}', t)$ is given by

$$\bar{u}(\mathbf{r}, \mathbf{r}', t) = \frac{1}{2\pi c_0^2} \int\limits_{-\infty}^{\infty} \omega^2 E_y^t(\mathbf{r}', \omega) \times G_b(\mathbf{r}, \mathbf{r}', \omega) P(\omega) \exp(-i\omega t) d\omega\,. \tag{74}$$

As shown in Sect. 2.3.2 and [11], the computation of the field transmitted through moderately rough dielectric interfaces can be carried out efficiently through the Gabor

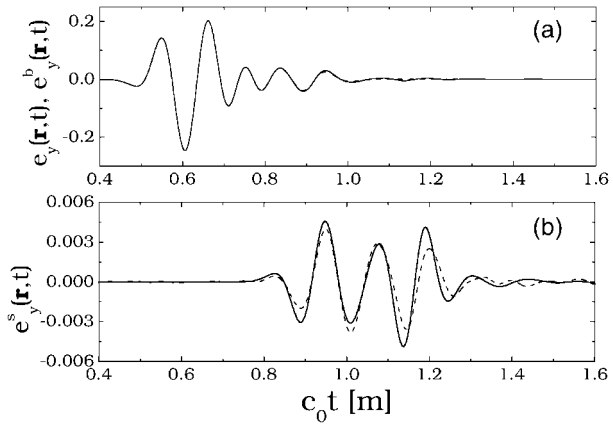

Fig. 12. Simulation results for scattered fields pertaining to Fig. 11. Parameters as in Fig. 4. Field observed at ($x = 0.3\,\mathrm{m}$, $z = 0.3\,\mathrm{m}$) (a): —— Total field e_y (reference solution); - - - Background field e^b_y (reference solution). Both are coincident on the scale of this drawing (i.e., the target-scattered field cannot be identified). (b): Target-scattered field $e^s_y = e_y - e^b_y$ (note the substantially enlarged amplitude scale). —— Reference solution; - - - Born-PB approximation (for implementation details, see [17]).

PO-PB algorithm. Moreover, these results can readily be extended to deal with the subsequent irradiation from an induced line-source in the dielectric halfspace, thereby yielding a *closed form* TD expression for the kernel in (74) similar to those in Sect. 2.3.2 and [11]. However, it may be computationally more efficient to synthesize the transmitted field E^t_y and the rough-surface halfspace Green's function G_b in the FD, and then compute the TD kernel in (74) via FFT algorithms [18] (see the discussion in [17]).

Numerical experiments have been conducted for the simulation configuration described in Fig. 11. A typical sample is shown in Fig. 12, which compares the Born-PB-generated result with a moment method rigorous reference solution. Reasonably good agreement is observed. For implementation details, see [17].

3. Inverse scattering

3.1 Overall problem strategy

In a further escalation of complexity, we have applied the Gabor PO-PB algorithms in Sects. 2.3 and 2.4 to the end-to-end imaging of subsurface environments in the presence of moderately rough interfaces, which is relevant for certain practical ground penetrating radar (GPR) scenarios, such as anti-personnel land mine remediation. Here, one typically is concerned with shallowly buried small targets having constitutive properties very close to those of the background soil; the interface-generated clutter may introduce severe constraints on target localization and classification capability. In this connection, *statistical* Monte-Carlo-based approaches for clutter suppression, which work reasonably well in detection problems with small roughness [19], turn out to be quite unreliable for localization and classification in the presence moderate roughness [20]. These considerations have motivated our recent investigations toward a more robust, physics-based, *adaptive* approach to subsurface imaging in the presence of a moderately (both in height and slope) rough air-soil interface. The NW-GB algorithm plays an important role in the efficient implementation of this approach, which has so far been applied to 2-D frequency-stepped [21, 22] and pulsed [17, 23] GPR configurations, for slightly lossy soils and low-contrast mine-like targets, yielding encouraging results.

The end-to-end strategy is set in the TD, utilizing suitable *time-windowing* of the data to perform *selective* imaging tasks [17]. Specifically [17], a prior (nonlinear) inverse scattering problem is solved to reconstruct the coarse-scale air-ground interface profile from sparse *early-time* observation data and the fast NW-GB forward scattering model (see Sect. 2.3). The resulting interface profile reconstruction is employed subsequently to correct the *late-time raw* observation data, compensating for ground reflection and (double) transmission; this yields significant clutter suppression. Target imaging is finally accomplished via robust inversion of the Born-linearized forward scattering model in Sect. 2.4. The problem geometry is shown in Fig. 11, with pulsed excitation. The underground test domain ($\mathcal{D}^{(test)}$ in Fig. 11) is to be imaged from sparse TD scattered field observations, so as to extract estimates of its dielectric properties which allow localization and classification of possible anomalies. To this end, the y-directed scattered electric field is sampled at N_t time instants at N_r fixed receiver locations $x^r_1, \ldots, x^r_{N_r}$ on the plane $z = z^r$ (Fig. 11) to obtain a set of observations. The *known term* in the problem is this set of $N_r \times N_t$ samples. In our numerical experiments, we shall use synthetic field observation data generated via a moment-method-based full-wave solution of the forward scattering problem (see [17] for details). Results for frequency-stepped GPR configurations are presented in [21, 22].

3.2 Reconstruction of the moderately rough dielectric interface profile

Following the problem strategy in Sect. 3.1, we consider the processing of the *early-time* response of a pulsed GPR system, sampled at a limited number of receivers, in order to extract the interface profile [23]. We use a compact low-dimensional spline parameterization of the roughness profile, which provides implicit regularization that mitigates the inherent ill-posedness of the problem, and then use the PO-PB forward scattering model in Sect. 2.3.2 and [11] to generate predictions of the reflected field at the receivers. The estimation problem is thus converted into a nonlinear optimization problem aimed at retrieving the unknown spline coefficients via minimization of a least-square error functional that

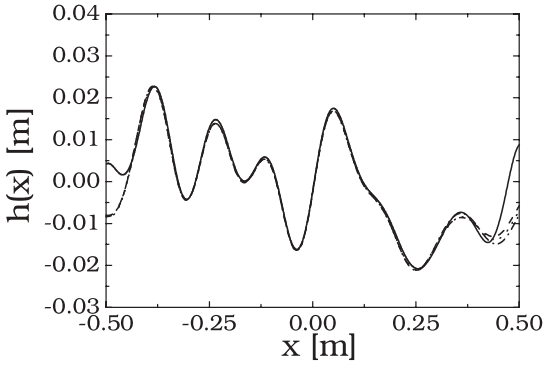

Fig. 13. Rough surface profile reconstruction via early-time response processing. Parameters as in Fig. 11. The early-time field at the receivers is sampled at $N_t = 50$ time instants with the observation windows chosen so as to roughly gate out causal scattering contributions from regions deeper than $\sim 8\,\mathrm{cm}$ below nominal ground. —— Actual profile; - - - Reconstruction with observation data corrupted by a $\pm 10\%$ additive uniform noise; ····· Reconstruction with -5% error in ϵ_{r1} and σ_1.

involves the PO-PB forward scattering prediction and the available observed data. The observation time windows are chosen so as to gate out the *late-time* response (i.e., causal contributions from regions beyond a critical depth) due to the possible presence there of buried targets which may produce a bias in the surface estimation. The resulting optimization problem is generally *non-convex*, and therefore the possible presence of local minima renders its numerical implementation non-trivial. Optimization strategies and computational issues are discussed in [23].

Referring to the geometry and parameters in Fig. 11, typical interface reconstruction examples are shown in Fig. 13. For these reconstructions, as discussed in [23], we used $N_t = 50$ time samples of the *early-time* response at each of the 11 receivers in Fig. 11; the observation time-windows were chosen so as to roughly gate out scattering contributions from possible regions deeper than $\sim 8\mathrm{cm}$ below nominal ground ($z = 0$), thus minimizing any possible bias due to target scattering. In order to test the robustness of the approach, we introduced some corruption into the observed data, as explained in the figure caption. The resulting cost functional was minimized using the conjugate gradient (CG) strategy described in [23], assuming as initial guess a flat interface at $z = 0$. Despite the polluted data, interface estimates are reasonably accurate, apart from the weakly-illuminated edge regions. This kind of accuracy was observed in many numerical experiments, with CG convergence typically achieved in $30 - 40$ iterations.

3.3 Imaging of targets buried below the moderately rough dielectric interface

The coarse-scale interface profile reconstruction in Sect. 3.2 is now used to generate predictions of the ground scattering, which is then suppressed so as to leave the *late-time* observed data primarily representative of the underground target scattering contribution. Our inversion strategy evolves from the Born-approximated NW-PB-parameterized problem formulation in (73), Sect. 2.4.2. Various *pixel-based* and *object-based* regularization techniques have been explored in order to achieve reliable inversion of the forward scattering model and to cope with its inherent *ill-posedness*. In pixel-based approaches, the test domain $D^{(test)}$ in Fig. 11 which is to be imaged, is discretized into N_p pixels. The resulting discretized linear forward model in (73) is cast into matrix form as

$$\underline{y} = \underline{\underline{A}} \cdot \underline{x} + \underline{n}\,, \tag{75}$$

where $\underline{y}$ is a column vector containing the observations (known term) in (73), $\underline{x}$ is a vector containing the *unknown* dielectric contrast $\Delta\epsilon_r$ at each pixel, $\underline{\underline{A}}$ is a matrix containing the space-time discretization of the Born TD kernel in (74), and the *noise* vector $\underline{n}$ accounts for measurement uncertainty and unmodeled irregularity effects. To reliably invert the linear model in (75), we have explored various *edge-preserving* regularization approaches. Those based on *total variation* (TV) [20] were found to be especially effective. In that procedure, the problem is posed as the minimization of the functional

$$J_{TV}(\underline{x}) = \left\| \underline{y} - \underline{\underline{A}} \cdot \underline{x} \right\|_2^2 + \beta_1 \left\| \underline{\underline{D}} \cdot \underline{x} \right\|_1^1 + \beta_2 \left\| K\left(\underline{x}\right) \right\|_2^2 . \tag{76}$$

In (76), the L^2-norm first term penalizes lack of data fidelity, while the other terms introduce some loose *a priori* knowledge about the object geometry, with β_1 and β_2 denoting regularization parameters. Thus, the second term highlights the expected piecewise smoothness in the reconstructed object function by penalizing the L^1 norm of a spatial gradient operator $\underline{\underline{D}}$. As compared with the L^2 norm in the standard Tikhonov regularization [24], the L^1 norm penalizes *large* jumps less, thus allowing sharper edges to form in the reconstructed object function and yielding visually better (less blurred) reconstructions. The last term in (76) is related to possible prior information about the object function sign. Assuming, for instance, a *negative* value for $\Delta\epsilon_r$ in the target region, the L^2 norm of the operator K penalizes *positive* values (or viceversa) of the reconstructed object function

$$\left[K\left(\underline{x}\right)\right]_k = \begin{cases} x_k, & x_k > 0\,, \\ 0, & x_k \le 0\,. \end{cases} \tag{77}$$

In our implementation, the cost functional in (76) is minimized via an iterative procedure based on half-quadratic approximations (see [25] for details). The choice of the regularization parameters β_1 and β_2 was implemented by trial and error.

Concerning *object based* reconstruction approaches, found to be particularly attractive was a *curve-evolution*

(CE) algorithm [26, 27, 28], wherein the target homogeneity is enforced explicitly, thereby reducing the imaging problem to estimating the target contour $\vec{C}$ and the relative permittivity contrast $\overline{\Delta\epsilon_r}$ via minimization of the following quadratic functional [28]

$$J_{CE}\left(\vec{C}, \overline{\Delta\epsilon_r}\right) = \frac{1}{2}\sum_n \left(e^s_{yn} - \overline{\Delta\epsilon_r} u_{yn}\right)^2 + \beta \int_{\vec{C}} d\ell \,. \tag{78}$$

The first term in (78) encourages data fidelity, with e^s_{yn} denoting space-time scattered field observation samples and u_{yn} denoting the corresponding forward model prediction for a given target contour $\vec{C}$ and unit-amplitude relative permittivity contrast. The second term serves as a regularizer by penalizing the arc-length of the estimated curve, with the regularization parameter β (empirically selected by trial and error here) affecting its smoothness. The cost functional in (78) is minimized in our implementation via CE using the level set method [29].

Referring to the geometry and parameters in Fig. 11, some representative reconstruction results are shown in Fig. 14. In these examples, the 20 cm × 20 cm square test domain surrounding the target to be imaged was discretized in 30×30 pixels, and $N_t = 300$ time samples of the *late-time* response (causally related to the test domain) were used. Specifically, the true object function (ground truth) is shown in Fig. 14a, and the corresponding TV and CE reconstructions are shown in Figs. 14b and c, respectively. Total variation (TV), though not yielding highly accurate point-wise reconstruction, provides reasonably accurate target *localization*. Curve evolution (CE) provides rather accurate direct estimations of *both* the target boundary *and* dielectric contrast. The limited viewing geometry renders the problem *more ill-posed* in the horizontal direction, resulting in less accurate horizontal localization in both cases. The effect of the interface roughness and the importance of adaptive compensation is highlighted in Fig. 14d, where a TV reconstruction *without* any compensation (i.e., assuming a flat interface at $z = 0$) is shown. The poor quality of the reconstruction can be only slightly improved using statistical processing, as shown in [20], but is still not comparable to that of Figs. 14b and c. The calibrated range of applicability of the implemented algorithm is discussed in [17]. Frequency-stepped GPR configurations are explored in [22].

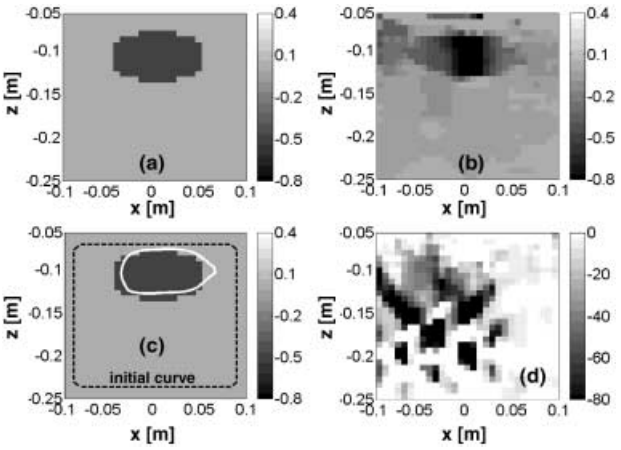

Fig. 14. Imaging results pertaining to the simulation domain and parameters in Fig. 11. Underground imaging examples ($N_t = 300$) with corrupted data (±10% additive uniform noise). For implementation details, see [17]. (a): Ground truth ($\Delta\epsilon_r$ reference configuration). (b): Total variation (TV) reconstruction with adaptive compensation. (c): Curve evolution (CE) reconstruction with adaptive compensation; estimated target boundary (white curve) is superposed on ground truth; estimated target permittivity: $\epsilon_{r2} = 3.56$, i.e., 1.7% error. (d): TV reconstruction without compensation (flat interface at $z = 0$).

4. Current and planned investigations, and alternative approaches

4.1 Current and planned investigations

The FD and TD algorithms discussed in Sects. 2 and 3 are restricted to 1-D aperture field distributions, and 2-D fields and physical configurations. Extensions to full 3-D vector fields and geometries are in progress. In this connection, systematic investigation of both rigorous and approximate (NW paraxially asymptotic) Gabor-based Gaussian beam (GB) parameterizations of time-harmonic 3-D vector wavefields radiated by 2-D large truncated plane aperture field distributions has been carried out in [30, 31]. These formulations have been subsequently extended to the TD in [32], for the case of NW-GBs. The FD quasi-real ray tracing scheme in [6, 7] and Sect. 3.1 has been extended to propagate 3-D vector fields through arbitrarily-shaped dielectric layers in [33]. In a stepwise approach toward the 3-D extension of the inverse scattering algorithms in Sect. 3, which should allow the treatment of more realistic GPR scenarios, we have started from NW-GB algorithms for scattering by, and transmission through, moderately rough 3-D dielectric interfaces. Preliminary results, for the TD case, have been presented in [34].

4.2 Alternative approaches

Although *all* applications presented in this review are based on the NW-GB Gabor discretization,there are recent alternative methodologies for GB-based algorithms. In [35], Rao and Carin proposed the method of matched pursuits (MP), a nonlinear iterative procedure for projection of a function onto a Gabor basis, in connection with forward and inverse scattering in electrically large inhomogeneous regions. For these applications, the MP method was found to provide better flexibility than the traditional Gabor decomposition of a fixed phase-space

lattice. Also, *frame-based* approaches have emerged as possible alternatives, which overcome some of the implementation difficulties associated with the conventional rigorous Gabor expansion [36, 37, 38]. These new rigorous schemes provide a different perspective for Gabor-parameterized field expansions. Their relation to the pragmatic approximate (but well calibrated) NW-GB schemes reviewed in this paper remains to be explored.

5. Conclusions

In this compact review, we have endeavored to document the accomplishments (so far) of the NW-GB algorithm for high-frequency FD and short-pulse TD operation, which are encouraging for those applications that meet certain "moderate" criteria. For the particular applications in this paper, these criteria have been specified in the text. Each new scenario needs to be attacked sequentially, starting with 2-D fields, calibrating the NW-GB algorithm against independent reference solutions, etc. This sequential approach has been illustrated here for the end-to-end imaging problem discussed in Sect. 3 and depicted in Fig. 11, which was synthesized by combining the constituent problems discussed in Sects. 2.1, 2.3, and 2.4. While this is a tedious process, the potential reward (if it works) is a physically appealing, highly efficient forward solver for assembling the massive data base required for forward predictions and inverse reconstructions in complex environments spanning large computational domains.

Acknowledgement. Work supported by ODDR&E under MURI grants ARO DAAG55-97-1-0013 and AFOSR F49620-96-1-0028, and by the Engineering Research Centers Program of the National Science Foundation under award number EEC-9986821. L.B. Felsen also acknowledges partial support from Grant No. 9900448 by the US-Israel Binational Science Foundation, Jerusalem, Israel, and from Polytechnic University, Brooklyn, NY 11201 USA.

References

[1] Hansen, T. B.; Yaghjian, A.: Plane-wave theory of time-domain fields: Near-field scanning applications. Piscataway (NJ): IEEE Press, 1999.

[2] Abramowitz, M.; Stegun, I. A.: Handbook of mathematical functions. New York (NY): Dover, 1964.

[3] Bastiaans, M. J.: Gabor's expansion of a signal into Gaussian elementary signals. Proc. IEEE **68** (1980), 538–539.

[4] Maciel, J. J.; Felsen, L. B.: Systematic study of fields due to extended apertures by Gaussian beam discretization. IEEE Trans. Antennas and Propagat. AP–**37** (1989), 884–892.

[5] Steinberg, B. Z.; Heyman, E.; Felsen, L. B.: Phase-space beam summation for time-harmonic radiation from large apertures. J. Opt. Soc. Am. A **8** (1991), 41–59.

[6] Maciel, J. J.; Felsen, L. B.: Gaussian beam analysis of propagation from an extended aperture distribution through dielectric layers, Part I – plane layer. IEEE Trans. Antennas and Propagat. AP–**38** (1990), 1607–1617.

[7] Maciel, J. J.; Felsen, L. B.: Gaussian beam analysis of propagation from an extended aperture distribution through dielectric layers, Part II – circular cylindrical layer. IEEE Trans. Antennas and Propagat. AP–**38** (1990), 1618–1624.

[8] Galdi, V.; B., F. L.; Castañon, D. A.: Narrow-waisted Gaussian beam discretization for two-dimensional time-dependent radiation from large apertures. IEEE Trans. Antennas and Propagat. AP–**49** (2001), 1322–1332.

[9] Galdi, V.; Felsen, L. B.: Two-dimensional pulsed propagation from extended aperture field distributions through planar dielectric layers via quasi-ray Gaussian beams. IEEE Trans. Antennas and Propagat. AP–**51** (2003), in press.

[10] Galdi, V.; Felsen, L. B.: Two-dimensional narrow-waisted Gaussian beam analysis of pulsed propagation from extended planar one-dimensional aperture field distributions through planar dielectric layers. – In: Ultra-Wideband, Short Pulse Electromagnetics – 6. Mokole, E. L. (ed.). New York, USA: Kluwer/Plenum Publishers, 2003, in press.

[11] Galdi, V.; Felsen, L. B.; Castañon, D. A.: Quasi-ray Gaussian beam algorithm for short-pulse two-dimensional scattering by moderately rough dielectric interfaces. IEEE Trans. Antennas and Propagat. AP–**51** (2003), in press.

[12] Galdi, V.; Felsen, L. B.; Castañon, D. A.: Quasi-ray Gaussian beam algorithm for time-harmonic two-dimensional scattering by moderately rough interfaces. IEEE Trans. Antennas and Propagat. AP–**49** (2001), 1305–1314.

[13] Chew, W. C.: Waves and fields in inhomogeneous media. Oxford: Oxford Press, 1996.

[14] Keller, J. B.: Accuracy and validity of the Born and Rytov approximations. J. Opt. Soc. Am. **59** (1969), 1003–1004.

[15] Habashy, T. M.; Groom, R. W.; Spies, B.: Beyond the Born and Rytov approximation: A nonlinear approach to electromagnetic scattering. J. Geophys. Res. **98** (1993), 1759–1775.

[16] Dasgupta, N.; Geng, N.; Dogaru, T.; Carin, L.: On the extended-Born technique for scattering from buried dielectric targets. IEEE Trans. Antennas Propagat. **47** (1999), 1739–1743.

[17] Galdi, V.; Feng, H.; Castañon, D. A.; Karl, W. C.; Felsen, L. B.: Moderately rough surface underground imaging via short-pulse quasi-ray Gaussian beams. IEEE Trans. Antennas and Propagat. AP–**51** (2003), in press.

[18] Press, W. H.; Teukolsky, S. A.; Vetterling, W. T.; Flannery, B. P.: Numerical recipes in C: The art of scientific computing, 2nd ed. Cambridge (UK): Cambridge Univ. Press, 1992.

[19] Dogaru, T. Collins, L.; Carin, L.: Optimal time-domain detection of a deterministic target buried under a randomly rough interface. IEEE Trans. Antennas Propagat. **49** (2001), 313–326.

[20] Feng, H.; Castañon, D. A.; Karl, W. C.; Miller, E. L.: GPR imaging approaches for buried plastic landmine detection. – In: Detection and Remediation Technologies for Mines and Minelike Targets V (Proc. SPIE, vol. 4038). Dubey, A. C.; Harvey, J. F.; Broach, J. T.; Dugan, E. R. (eds.). Orlando, FL, USA: SPIE, 2000, 1485–1496.

[21] Galdi, V.; Castañon, D. A.; Felsen, L. B.: Multifrequency reconstruction of moderately rough interfaces via quasi-ray Gaussian beams. IEEE Trans. Geosci. and Remote Sensing **40** (2002), 453–460.

[22] Galdi, V.; Feng, H.; Castañon, D. A.; Karl, W. C.; Felsen, L. B.: Multifrequency subsurface sensing in the presence of a moderately rough air-soil interface via quasi-ray Gaussian

beams. Radio Science, Vol. 37, No. 6, Nov.–Dez. 2002. Online: DOI 10.1029/2001RS002557, citation no. 8007.
[23] Galdi, V.; Pavlovich, J.; Castañon, D. A.; Karl, W. C.; Felsen, L. B.: Moderately rough dielectric interface reconstruction via short-pulse quasi-ray Gaussian beams. IEEE Trans. Antennas and Propagat. AP–**51** (2003), in press.
[24] Bertero, M.: Linear inverse and ill-posed problems. – In: Advances in Electronics and Electron Physics, Vol. 75. San Diego: Academic Press, 1989, 1–20.
[25] Vogel, C. R.; Oman, M. E.: Fast, robust total variation-based reconstruction of noisy, blurred images. IEEE Trans. Image Processing **7** (1998), 813–824.
[26] Yezzi, A.; Kichenassamy, S.; Kumar, K.; Olver, P.; Tennenbaum, A.: A geometric snake model for segmentation of medical imagery. IEEE Trans. Medical Imaging **16** (1997), 199–209.
[27] Shah, J.: Riemannian drums, anisotropic curve evolution, and segmentation, J. Visual Communication and Image Representation, **11** (2000), 142–153.
[28] Feng, H.: Curve evolution object-based techniques for image reconstruction and segmentation. Dissertation. Boston, MA, USA: Boston University, 2002.
[29] Osher, S.; Sethian, J.: Fronts propagation with curvature dependent speed: Algorithms based on Hamilton-Jacobi formulations. J. Comp. Phys. **79** (1988), 12–49.
[30] Maciel, J. J.; Felsen, L. B.: Discretized Gabor-based beam algorithm for time-harmonic radiation from two-dimensional truncated planar aperture distributions – I: Formulation and solution. IEEE Trans. Antennas and Propagat. AP–**50** (2002), in press.
[31] Maciel, J. J.; Felsen, L. B.: Discretized Gabor-based beam algorithm for time-harmonic radiation from two-dimensional truncated planar aperture distributions – II: Asymptotics and numerical tests. IEEE Trans. Antennas and Propagat. AP–**50** (2002), in press.
[32] Galdi, V.; Felsen, L. B.; Castañon, D. A.: Time-domain radiation from large two-dimensional apertures via narrow-waisted Gaussian beams. IEEE Trans. Antennas and Propagat. AP–**50** (2002), in press.
[33] Maciel, J. J.; Felsen, L. B.: Gabor-based narrow-waisted Gaussian beam algorithm for transmission of aperture-excited 3D vector fields through arbitrarily shaped 3D dielectric layers. Radio Science, Vol. 37, No. 6, Nov.–Dez. 2002. Online: DOI 10.1029/2001RS002556, citation no. 8005.
[34] Galdi, V.; Felsen, L. B.; Castañon, D. A.: 3-D short pulse scattering by moderately rough dielectric interfaces via quasi-ray Gaussian beams. Proc. 2002 IEEE Antennas and Propagat. Int. Symposium, vol. 4, San Antonio, TX, USA, June 16–21, 2002. 252–255.
[35] Rao, B.; Carin, L.: Beam-tracing-based inverse scattering for general aperture antennas. J. Opt. Soc. Am. A **16** (1999), 2219–2231.
[36] Arnold, J. M.: A localised beam representation of high-frequency wavefields using the Daubechies-Wilson basis. Proc. URSI Electromagnetic Theory Symposium, Victoria, BC, Canada, May 13–17, 2001. 53–55.
[37] Letrou, C.; and Lugara, D.: A frame based and beam launching method for lens antennas modeling and optimization, Proc. URSI Electromagnetic Theory Symposium, Victoria, BC, Canada, May 13–17, 2001, 59–61.
[38] Shlivinski, A.; Heyman, E.; Boag, A.; Lugara, D.; Letrou, C.: Gabor-frame phase space beam summation formulation for wideband radiation from extended apertures, Proc. URSI Electromagnetic Theory Symposium, Victoria, BC, Canada, May 13–17, 2001, 56–58.

Leopold B. Felsen was born in Munich, Germany, on May 7, 1924. He received the B.E.E. (*summa cum laude*), M.E.E, and D.E.E. degrees from the Polytechnic Institute of Brooklyn, Brooklyn, NY, in 1948, 1950, and 1952, respectively. He emigrated to the United States in 1939 and served in the U.S. Army from 1943 to 1946. After 1952 he remained with the Polytechnic (now Polytechnic University), gaining the position of University Professor in 1978. From 1974 to 1978 he was Dean of Engineering. In 1994 he resigned from the full-time Polytechnic faculty and was granted the status of University Professor Emeritus. He is now Professor of Aerospace and Mechanical Engineering and Professor of Electrical and Computer Engineering at Boston University, Boston, MA (part-time). He is the author or coauthor of over 350 papers and of several books. Dr. Felsen is a member of Sigma Xi, a Life Fellow of the IEEE, and a Fellow of the Optical Society of America and the Acoustical Society of America. He has held named Visiting Professorships and Fellowships at universities in the United States and abroad, including the Guggenheim in 1973 and the Humboldt Foundation Senior Scientist Award in 1981. In 1974 he was an IEEE/APS (Antennas and Propagation Society) Distinguished Lecturer. He was awarded the Balthasar van der Pol Gold Medal from the International Union of Radio Science (URSI) in 1975, an honorary doctorate from the Technical University of Denmark in 1979, the IEEE Heinrich Hertz Gold Medal for 1991, the APS Distinguished Achievement Award for 1998, the IEEE Third Millenium Medal in 2000 (nomination by APS), an honorary Laurea degree from the University of Sannio, Benevento, Italy, 2003, the IEEE Electromagnetics Award for 2003, three Distinguished Faculty Alumnus Awards from Polytechnic University, and an IEEE Centennial Medal in 1984. Also, awards have been bestowed on several papers authored or coauthored by him. In 1977 he was elected to the National Academy of Engineering. He has served on the APS Administrative Committee from 1963–1966, and as Vice Chairman and Chairman for both the United States (1966–1973) and the International (1978–1984) URSI Commission B.

Vincenzo Galdi was born in Salerno, Italy, on July 28, 1970. He received the *Laurea* degree (*summa cum laude*) in Electrical Engineering and the Ph.D. degree in Applied Electromagnetics from the University of Salerno, Italy, in 1995 and 1999, respectively. From April to December 1997, he held a visiting position in the Radio Frequency Division of the European Space Research & Technology Centre (ESTEC-ESA), Noordwijk, The Netherlands. From September 1999 to August 2002, he held a research associate position in the Department of Electrical and Computer Engineering at Boston University, Boston, MA. In November 2002, he was appointed Associate Professor of Electromagnetics, and joined the Department of Engineering at the University of Sannio, Benevento, Italy, where he is currently working. Dr. Galdi is the recipient of a 2001 International Union of Radio Science (URSI) "Young Scientist Award".